Durability and self-healing of engineered cementitious composites exposed to simulated sewage environments

Tianyu Wang [a,b], Duo Zhang [a], He Zhu [a], Baosong Ma [c], Victor C. Li [a,*]

[a] Department of Civil and Environmental Engineering, University of Michigan, Ann Arbor, MI, 48109, USA
[b] College of Engineering, China University of Geosciences-Wuhan, Wuhan, Hubei Province, 430074, China
[c] School of Civil Engineering, Sun Yat-Sen University, Zhuhai, Guangdong Province, 519082, China

ARTICLE INFO

ABSTRACT

Corrosion factors including microbiologically induced corrosion accelerate cracking and deteriorations in a sewer concrete pipe especially in regions close to the pipe crown and that near the waterline. Engineered cementitious composites (ECC) is a novel class of ductile cement-based composites and possesses autogenously tight cracks and robust self-healing conducive to sewage environments resistance. This paper presents an experimental study on the durability of ECC exposed to sewage environments simulated by treatments including sulfuric acid exposure and physical erosion. The physical and mechanical properties of ECC were examined in relation to those of fiber-free mortar specimens as control. The objective of this research is to establish fundamental knowledge on the behavior of ECC under aggressive sewage environments. Results showed that the permeable voids increased, and the strength decreased for both ECC and mortar. However, the residual compressive and tensile strength of ECC were 30–65% and 300–370% higher than those of the mortar group after 12 corrosion cycles, respectively. After corrosion cycles, the length change ratio of ECC was about 20% of that of the control, which indicates that ECC has better dimensional stability under the corrosive conditions. Further, self-healing of microcrack damage was observed in ECC under all exposure conditions in this study. It is concluded that ductile ECC has significant advantages in mechanical and durability performance over conventional brittle mortar/concrete under the simulated environments unique in sewage lines. This research generates new data that establish ECC as a durable material for sewer pipeline construction and rehabilitation.

1. Introduction

Concrete sewer pipes are prone to performance degradation in corrosive environments including microbiologically induced corrosion (MIC) [1]. The MIC process follows three typical stages: H_2S formation, biogenic sulfuric acid accumulation, and acid-induced concrete deterioration [2–4]. During the first stage, sulfide in the sewage pipe transforms into H_2S gas by sulfate reducing bacteria (SRB) under the waterline [5]. The released H_2S provides a sulfur source for biogenic sulfuric acid generation [6,7] caused by sulfur oxidizing bacteria (SOB), thus lowering the environmental pH to 1–2 [8,9]. The low pH, together with the sulfate anions, dissolves cement hydration products such as calcium silicate hydrate (CSH) [10] and promotes the formation of expansive ettringite (AFt) and gypsum that accelerate cracking and disintegration [11,12]. Several approaches have been developed for

simulating the MIC process in laboratory conditions. Biogenic sulfuric acid was prepared as the corrosive agent in Ref. [13]. To better reproduce the microorganisms and sulfate concentrations that closely resemble the in-situ environment, the "Hamburg chamber" and other simulation chambers were developed [8,14,15]. However, the relationship between the corrosion that occurred in simulation chambers and in-situ conditions remained unclear [16].

Field investigations found that concrete experienced accelerated deterioration in the vicinity of the crown and sewage waterline [17,18]. The crown area has the highest H_2S concentration which is the cause of the accelerated deterioration [19]. Concerning the rapid corrosion around the waterline, it is assumed to be caused by the migration of the acid from the upper region, and by the removal of the corrosion products by flow erosion and the wet-dry cycles [20,21]. Experimental studies reproducing the concrete corrosion around the sewer waterline have not

---

Table 1

Chemical compositions (in %) of Portland cement and fly ash.

Oxide Chemistry	SiO$_2$	Al$_2$O$_3$	SO$_3$	MgO	P$_2$O$_5$	K$_2$O	TiO$_2$	Fe$_2$O$_3$	CaO	Cl	Loss on ignition
PC	19.19	15.4	2.54	3.46	–	0.07	0.39	2.13	54.79	–	2.03
FA	38.56	17.92	1.86	4.35	1.12	0.97	1.24	2.13	20.92	0.01	3.78

Table 2

Properties of PVA fiber.

Length (mm)	Diameter (μm)	Elongation (%)	Density (kg/m^3)	Young's modulus (GPa)	Tensile strength (GPa)	Oil coating (%)
8	39	6	1300	42.8	1.6	1.2 by mass

Table 3

Mixture proportions of ECC and cement mortar (mass ratio).

Mixture ID	Cement (PC)	FA	Sand	Water	SP	Fiber
ECC	1	3.5	0.8	0.25	0.094%	2 vol%
Mortar	1	3.5	0.8	0.25	0.094%	–

been reported in the literature. Although full-scale experiments and in-situ exposure tests can be valuable, the variations from one site to another reduce the general applicability of the experimental data and findings [16]. The lack of widely accepted standards and construction practice guidance also leads to the dilemma of reproducing the corrosion process under sewer environments [22,23]. In general, the damage caused by the MIC process can be explained as acids attacking the concrete matrix, and sulfuric acid was a widely used and typical way to reproduce the chemical aspect of the MIC process in laboratory tests [14, 24,25]. Therefore, sulfuric acid was chosen as the corrosive medium in this study. A simulated erosion process (physical removal of the corroded layer), and dry-wet cycles were incorporated to further simulate the unique sewer environment near the waterline.

The modification and rehabilitation of deteriorated underground concrete structures can be problematic in dense urban communities [26, 27]. To solve this problem, various approaches have been investigated to improve concrete resistance against the sewage environments. Calcium aluminate cement (CAC) was applied to sewer concrete pipes because of their better resistance to biogenic acid [28]. Supplementary cementitious materials (SCMs) such as ground granulated blast-furnace slag (GGBS), fly ash and silica fume have been considered for concrete corrosion resistance by decreasing the porosity and permeability [17]. In addition, antimicrobial agents that could inhibit microorganisms (SOB, e.g., Thiobacillus thioparus) and then reduce the biogenic acid production have been incorporated as additives to concrete [16,29]. Despite these attempts, effective control of concrete pipe deterioration under sewer environment has not been found [30]. Most of the previous studies were based on traditional concrete materials [31,32]. The intrinsic brittleness of concrete materials aggravates the cracking and structural failure [33] and represents a major challenge for traditional sewer pipes.

Engineered cementitious composites (ECC) is a class of fiber-reinforced cementitious composites featuring ultrahigh tensile ductility. The designed mechanical interactions between the fiber and matrix enable the tensile strain-hardening and multiple-cracking behavior of ECC [34]. Moreover, ECC maintains low water permeability even beyond the elastic stage due to its intrinsically tight crack width and self-healing behavior [35,36]. These characteristics enhance the durability of ECC under a variety of aggressive environments [37, 38]. For example, Liu et al. [39] found that ECC retained 6.3 MPa tensile strength and 2.1% tensile strain after exposure to sulfate and sulfate-chloride solution for 420 days. ECC containing 6% MgO was demonstrated to resist sulfuric acid in acid mine drainage (AMD) [40]. Ohno and Li [41] found that the deflection capacity of ECC increased after sulfuric acid exposure. The self-healing property of ECC was

observed under the sulfate and chloride environment [42]. However, corrosive environments in these previous studies were limited to simple acid/salt solution soaking which did not realistically represent the unique sewer environment. In this paper, it is hypothesized that ECC can mitigate the corrosion process in sewer structures. Apart from sulfuric acid and sulfates exposure, additional factors including dry-wet cycle, "active acid" attack (with pH maintained over time as explained in Section 2.2) and physical removal of corrosion layer were considered for the first time [14,43,44], to obtain a comprehensive understanding of ECC's behavior in the sewer environment.

In this study, the durability performance of ECC and fiber-free mortar (as control) under a set of simulated corrosive sewage environments was experimentally investigated. The mortar with a 28d compressive strength of 30–35 MPa was chosen to represent common sewer concrete materials which has compressive strength of 30–50 MPa [45]. The ECC material with fiber reinforcement was designed based on the same matrix as the mortar for the control group. The fundamental difference in mechanical property between these two materials is that ECC possesses a tensile strain capacity several hundred times that of mortar. The deterioration mechanisms of the two cementitious materials under the simulated sewage corrosive environments were assessed through changes in visual appearance, tensile properties, compressive strength, and length dimension. Besides, the permeable voids, pH value variation of the acid soaking solution, corrosion layer and self-healing product were studied to lay a better foundation for understanding the damage caused by the simulated sewage environments. The objective of this research is to develop fundamental knowledge of the behavior of ECC under aggressive sewage corrosive environments. The results are expected to guide the design of durable pipelines against the typical aggressive corrosive process in sewage systems.

2. Materials and methods

2.1. Materials, mix proportions, and specimen preparation

Portland cement (PC, Lafarge Holcim) conformed to ASTM C150 [46], Class C fly ash (FA, Boral Material Technologies) conformed to ASTM C618 [47], silica sand (US Silica, F75), superplasticizer (SP, MasterGlenium 7920, BASF), and tap water (TW) were used to prepare the ECC and mortar specimens. The chemical compositions of PC and FA are listed in Table 1. The average and maximum grain diameter of the silica sand was 75 μm and 200 μm, respectively.

For the ECC, polyvinyl-alcohol (PVA, Kuraray RECS 15) fiber was included as reinforcement. The properties of the PVA fiber are listed in Table 2. Table 3 lists the mix proportions of the PVA fiber-based ECC and the fiber-free mortar. All specimens were made with the same matrix composition while 2 vol% PVA fiber was used in the ECC.

PC, FA and sand were added into a 12-L Hobart mortar mixer and dry mixed at 100 rpm for 5 min. Then 2/3 and 1/3 of the water and SP solution were added step by step into the solid ingredients with each addition accompanied by a 3-min mixing. After that, the fresh mixture was cast into the molds as the Mortar group and vibrated for 30 s on a

Table 4
Details of specimens used in this study.

Test purpose	Specimen type	Specimen size (mm × mm × mm)	Quantity in total/ Material type
Visual appearance & Corrosion layer	Small cube	50 × 50 × 50	108 ECC & 108 mortar
Permeable voids	Large cube	70.7 × 70.7 × 70.7	117 ECC & 117 mortar
Compressive strength	Small cube	50 × 50 × 50	234 ECC & 234 mortar
Tensile properties	Dogbone shaped	As described in [48]	234 ECC & 234 mortar
Length change	Prism	25 × 25 × 300	36 ECC & 36 mortar
Self-healing	Dogbone shaped	As described in [48]	18 ECC

vibration table. For the ECC group, the PVA fiber was added into the fresh mortar mixture and mixed for another 5 min. The fresh ECC mixture was then cast into the molds and vibrated for 30 s. A plastic sheet covered the specimens for 24 h before demolding. The demolded specimens were stored in air at a temperature of 20 °C for 28 days before testing.

Table 4 summarizes the details of the specimens prepared for this study, including the type, dimensions, sample size, and test purpose. All specimens were exposed to the three exposure conditions described in Section 2.2 below.

Details of the exposure conditions are described in Section 2.2. The 70% sulfuric acid from Fisher Scientific was used to prepare the 1% H_2SO_4 solution. The most representative chemical species of the sewage flow include the sulfate and sulfide ions (i.e., SO_4^{2-}, S^{2-}) which provide

the source of sulfur for the MIC process. To emulate this chemical environment, sodium sulfate and sodium thiosulfate from Fisher Scientific were used to formulate the sewage solution [49].

2.2. Exposure conditions

Three exposure conditions were considered for the durability evaluation as shown in Fig. 1. Condition I simulated the exposure condition of the waterline area in a sewage pipe, while Condition II simulated that of the crown area. Condition III was used as a control with specimens exposed to tap water. For each condition, a 7-day-cycle was adopted. All specimens were exposed up to twelve cycles.

Condition I was comprised of three stages. In the first stage, to simulate the exposure to biogenic acid, all specimens were exposed to 1% H_2SO_4 solution for three days. The second stage simulated the sewage water level rise and immersion of the H_2SO_4-corroded area, such that the corrosion product might be dissolved or washed away (i.e., eroded) by the sewage flow [16,50]. For this stage, the specimens were set in the simulated sewage for 3 days. Following [49], the main sulfate concentration in the simulated sewage was designed as 170 mg/L SO_4^{2-} and 30 mg/L S^{2-} by adding Na_2SO_4 and $Na_2S_2O_3$. The simulated sewage was replaced with a new solution after every cycle to maintain the sulfate concentration. For specimens in Condition I, the "erosion process" was simulated by mechanical sanding using a 3 M 346U Paper (3 M Company) as shown in Fig. 2 [16]. One of the six surfaces of the cube specimen was set as the "corrosion surface". The corrosion surface should always be kept as the top side of the cube in the corrosive liquid without shelter. The simulated erosion was applied to the corrosion surface of the cube specimen, the four rectangular surfaces of the prism specimen and the flat surfaces of the dogbone shaped specimen to ensure
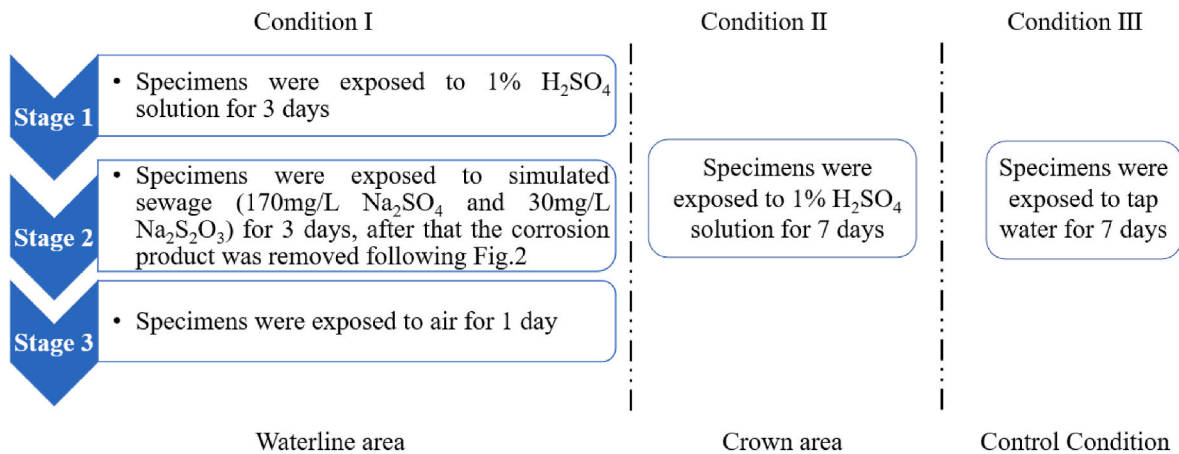

Condition I

Stage 1	• Specimens were exposed to 1% H_2SO_4 solution for 3 days
Stage 2	• Specimens were exposed to simulated sewage (170mg/L Na_2SO_4 and 30mg/L $Na_2S_2O_3$) for 3 days, after that the corrosion product was removed following Fig.2
Stage 3	• Specimens were exposed to air for 1 day

Waterline area

Condition II

Specimens were exposed to 1% H_2SO_4 solution for 7 days

Crown area

Condition III

Specimens were exposed to tap water for 7 days

Control Condition

Fig. 1. Exposure conditions for each 7-days-cycle of durability testing.

a — A horizontal force was provided to push the specimens forward 10 cm / Sandpaper
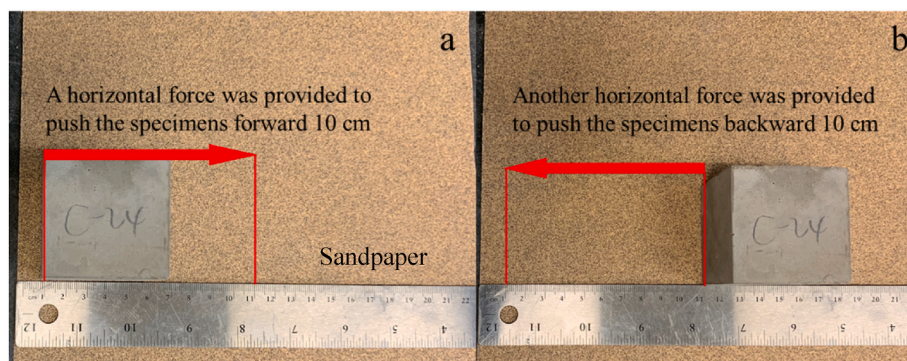b — Another horizontal force was provided to push the specimens backward 10 cm

Fig. 2. Surface erosion was conducted for 50 times in each cycle of durability testing under Condition I Stage 2.
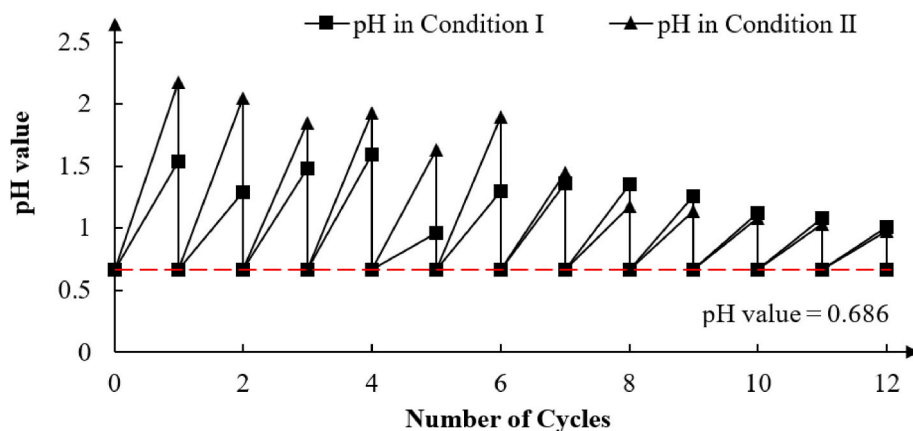
Fig. 3. Measured pH variation of the "active acid" solution in Conditions I and II.
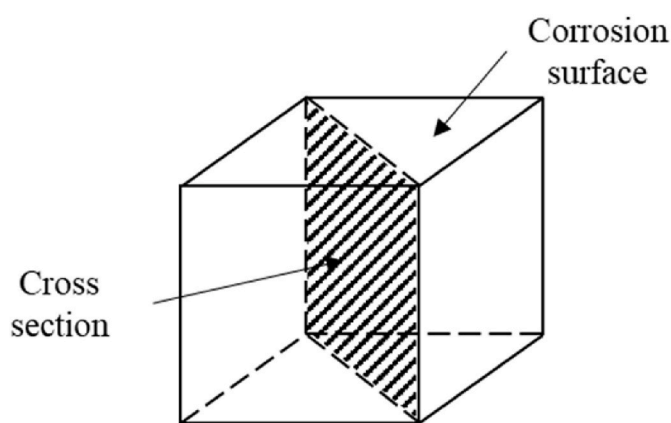

Fig. 4. Cross sectional cut for the corrosion damage characterization.

that each specimen in one specimen type experienced erosion effect based on its own weight. The final stage simulates the sewage flow level drop and the drying of the concrete surface. For this Stage 3, the specimens were placed in a fume hood and dried for 24 h.

Condition II was designed to simulate the pipe crown area so that specimens were fully immersed in the 1% H_2SO_4 solution for seven days. Condition III was designed as the control condition in which specimens were exposed to tap water for seven days.

In this experimental work, the pH of the acid solution in Conditions I and II was maintained at 0.67 by replenishing 70% sulfuric acid after each cycle to simulate the "active acid attack" in the MIC process in sewage environment [51]. The pH value variation of the "active acid" solution pH (Fig. 3) was measured by Hanna Instruments HI 9313–6 portable pH/EC meter. The solid-liquid volume ratio was maintained at 1:50.

2.3. Material characterization after exposures

Visual appearance and corrosion layer characterization: After exposing to Conditions I and II, the small cube specimens were found to develop a corroded layer consisting of the white zone and brown zone from the surface to core. The specimens were cut along the diagonal perpendicular to the corrosion surface of the 50 × 50 × 50 mm cube specimen to obtain a cross-section for damage observations (Fig. 4). The residual corrosion layer was observed and measured on these cross-sections using an Infinity X–C21 electron microscope and a vernier caliper. Eighteen small cube specimens (6 for each condition) were prepared for the residual corrosion layer observation and measurement every two cycles. Before the cutting process, the visual appearances of the

specimens exposed to all conditions were recorded based on the corrosion surfaces of the small cube specimens after 4 and 12 corrosion cycles, using a digital camera.

Permeable void characterization: The evolutions of permeable voids in ECC and mortars were measured based on the larger 70.7 × 70.7 × 70.7 mm cube specimens (3 specimens for each test) according to ASTM C642 [52]. The corrosion layer that completely debonded from the specimen were removed before the test.

Compression and tensile property characterization: After each cycle of exposure condition, eighteen 50 × 50 × 50 mm cube specimens (6 for each condition) and eighteen dogbone-shaped specimens (6 for each condition) were randomly selected for the compression and tension tests. The corrosion layer that completely debonded from the specimen were removed before the compression and tension test. The compression test was conducted on the small cube specimens using a FORNEY F-96 machine at a loading rate of 0.3 MPa/s according to ASTM C109/C109 M [53]. The corrosion surface was kept upward as the loading face. The compressive strength was calculated by dividing the peak load by the actual cross-sectional area measured before testing. The tensile test was performed on the dogbone-shaped specimens using an Instron machine (ElectroPlus E10000 Linear-Torsion Model) [54] at a loading rate of 0.5 mm/min. Two linear variable displacement transducers (LVDTs) with an 80 mm gauge length were used to measure the deformation of the specimens.

Length change characterization: Prism specimens (12 for each exposure condition, 36 specimens in total) were used to determine length changes under each of the three exposure conditions. The square faces at both ends of the specimens were sealed with epoxy resin to ensure that no deterioration would occur in the part of the specimens in contact with the comparator. The length change was recorded after each treatment cycle according to ASTM C490/C490 M−17 [48]. To understand the mechanism behind the observed macroscopic length change, scanning electron microscopy (SEM using a JEOL IT500) and energy dispersive spectroscopy (EDS) analyses were conducted. Six 5 × 5 × 2 mm solid samples were collected from the corroded layer after corrosion cycles. The secondary electrons images were acquired at a 4000x magnification under a 10 kV accelerating voltage.

Self-healing behavior characterization: The self-healing phenomenon in ECC was monitored by resonant frequency (RF) measurements according to ASTM C215 [55,56]. Eighteen dogbone shaped specimens (6 for each exposure condition) were prepared for the self-healing behavior characterization by preloading to a tensile strain of 1%. The RF values were measured before and after preloading and were subsequently measured after each exposure cycle. The open cracks and the sealed cracks after self-healing were recorded by the Infinity X–C21 microscope. For the X-ray diffraction (XRD, Rigaku SmartLab) test, the self-healing and corrosion product were collected from the sealed crack
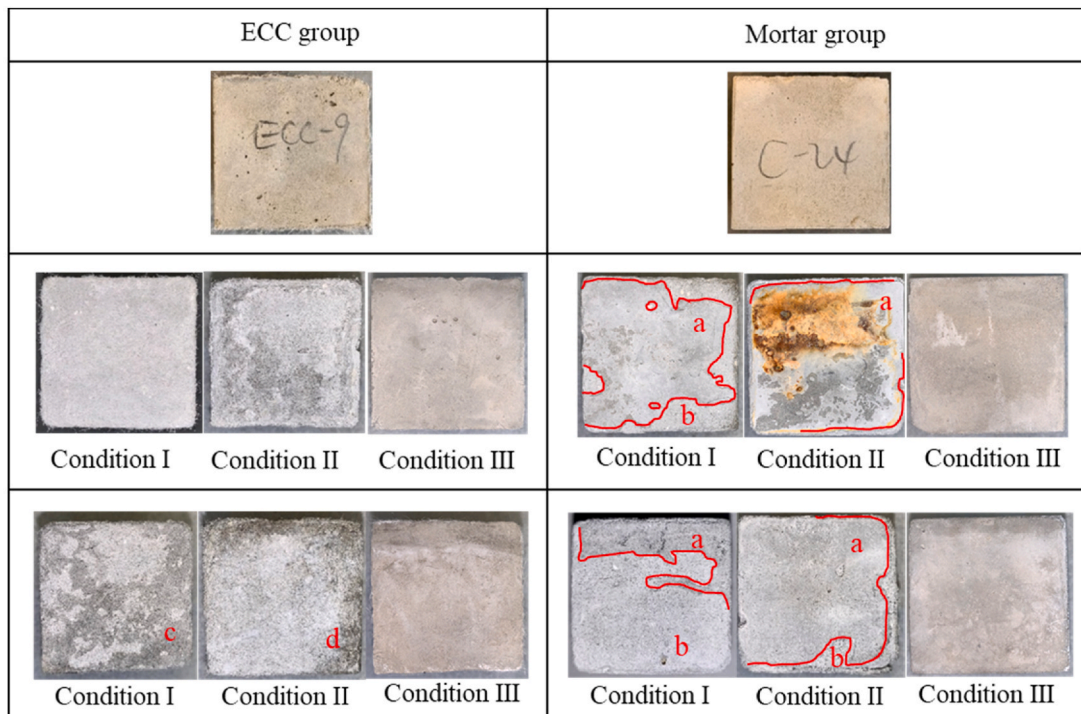
Fig. 5. Under Conditions I and II, the corrosion surface of the mortar specimens revealed corroded layer without spalling (marked "a") and exposed matrix after spalling (marked "b"). In contrast, ECC showed no spalling. Instead, only discolored surface and abrasion caused by corrosion-erosion (marked "c"), and corrosion product (marked "d") can be observed. No surface damage was observed in ECC or mortar under Condition III.
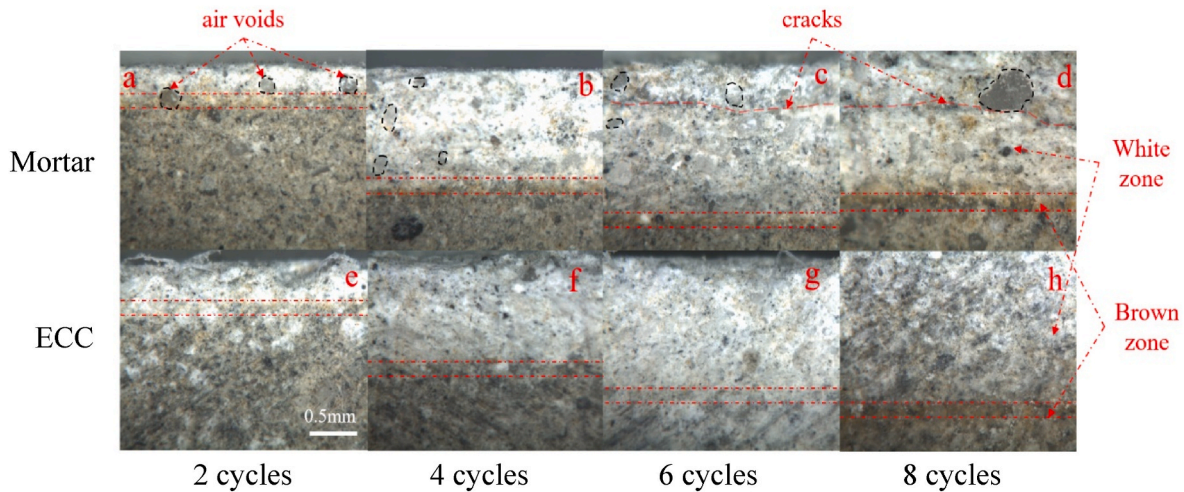

Fig. 6. Typical cross-sectional view showing corrosion layer in mortar and ECC specimens after 2, 4, 6, and 8 corrosion cycles under Condition II with the corrosion front (marked by the double dashed line) moving down towards the inner matrix with increasing exposure cycles. Only part of the corroded layers is shown in (d) and (h) as they are too thick to be presented in one single image.

and corroded surface layer, respectively. Then, the samples were ground into powder with a mortar. More than 1.0 g powder samples were prepared for each XRD test. The samples were front-loaded and scanned in 5–60° 2θ (step size 0.02° 2θ) under X-ray generated by a CuKα radiation.

3. Results and discussion

3.1. Visual appearance and corrosion layer characterization

The visual appearance of the corrosion surface (Fig. 5) of the small cube specimens was examined after exposure to simulated sewage environments. This is also the surface artificially eroded under Condition I

exposure. Except for the specimens in tap water (Condition III), deterioration was observed on both mortar and ECC specimens after 12 cycles exposure to Conditions I or II.

Under Condition I, the simulated corrosion-erosion process caused visible surface abrasion to both mortar and ECC specimens. The corroded surface layer of the mortar specimen showed partial spalling (marked as "b" in Fig. 5), with the remaining corroded material (marked as "a" in Fig. 5) loosely attached to the inner matrix. In contrast, ECC revealed discoloration and abrasion (marked as "c" in Fig. 5) but with no spalling on the surface. The enhanced mechanical integrity revealed in the ECC specimens, even upon exposure to the severe combined corrosion-erosion environment, stems from the tensile ductility of ECC
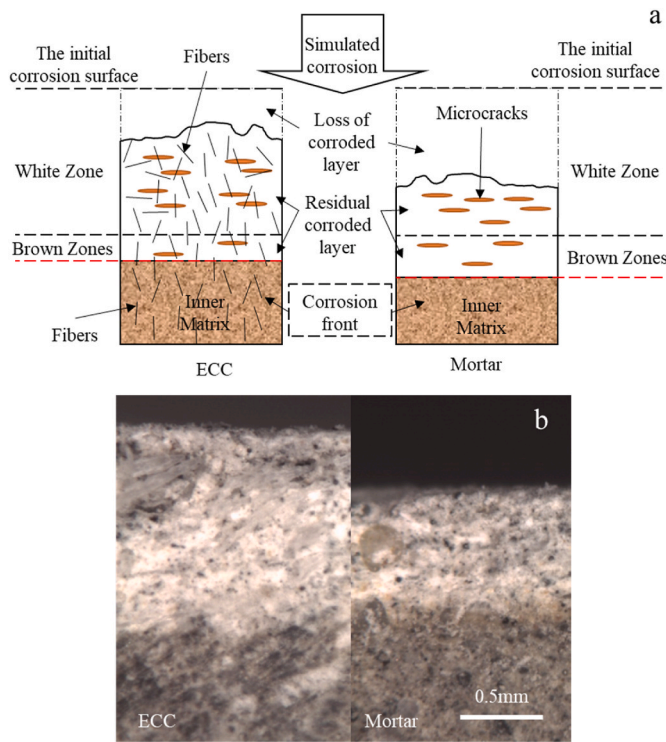
Fig. 7. (a) The residual corroded layer thickness of the mortar group is smaller than that of the ECC group because of poorer mechanical stability under corrosive conditions. With increased number of exposure cycles, the corrosion front moves inwards towards the inner matrix. (b) Sectional view of the corroded layer of ECC and Mortar specimens after 4 cycles in Condition I.

material [57].

Under Condition II, despite no imposed artificial erosion, delamination of the weak corroded layer, loosened material, and localized spalling were observed on the mortar specimen surface. This indicated that the "active acid attack" and the expansive corrosion product brought serious damage to the mortar. For the ECC specimens, white corrosion products (mainly $CaSO_4$) were observed (marked as "d" in Fig. 5) on the surface, distinct from the discoloration and abrasion caused by corrosion-erosion in Condition I. No significant spalling and loosened material could be observed in the ECC specimens under Condition II, suggesting a more stable corrosion layer [58] in the ECC specimens. This is also illustrated in Fig. 6, which shows the damage

condition revealed in an approximately 4 × 5 mm area of the cross-sectional cut (Fig. 4) near the corrosion surface of the small cube specimens.

A corroded layer of several mm thick typically forms on the surface of the specimens under acid attack [59]. Specimens under Condition II without the erosion effect were chosen for further study. The corroded layer (Fig. 6) can be visually divided into two parts in the specimen cross-section: white zone and brown zone. The white zone mainly consists of SiO_2 and $CaSO_4 \cdot 2(H_2O)$ (white corrosion product). The brown zone consists of ferric hydroxide that accounts for the brown color [60]. Brown spots invading the white zone can be observed in the transition region defined by a pair of red lines. Cracks can be observed in the cross-section in the mortar group (e.g. (c) and (d)). In contrast, the corroded layer of the ECC group appears denser and intact.

The residual thickness of the corroded layer (corroded layer thickness minus the eroded layer thickness, Fig. 7) was measured at six different points in the horizontal direction. The average value was calculated after removing the maximum and minimum values and plotted as a function of the exposure cycles in Fig. 8. The residual corroded layer thickness of all the specimens grew as the number of cycles increased. For mortar specimens, the corrosion layer became looser and had a higher tendency to spall due to erosion and corrosion as illustrated in Fig. 7. The residual corroded layer of mortar specimens was 2.35 mm and 2.79 mm after 12 cycles under Conditions I and II, respectively. For ECC specimens, fiber reinforcement stabilizes the corrosion layer. After 12 cycles in Condition I and II, ECC specimens had thicker 3.03 mm and 3.15 mm residual corroded layer, respectively. The difference in residual corroded layer thickness of ECC (0.12 mm) after 12 cycles in Condition I and II was 72.7% lower than that of the mortar (0.44 mm). This shows that ECC had better resistance to corrosion-erosion damage over the control mortar.

It was difficult to determine the actual corrosion depth of the ECC or mortar specimens because of the different thickness losses (Fig. 7). According to Ref. [44], the corrosion layer acts as a protective barrier between the corrosive environments and the intact matrix. It is hypothesized that the intact matrix of ECC was better protected by the thicker protection barrier compared to the control mortar. Furthermore, the unique tensile ductility of ECC may have contributed to the better resistance to the corrosive conditions compared to mortar. Further studies are needed to evaluate this hypothesis.

3.2. Permeable voids

Large cubes (70.7 × 70.7 × 70.7 mm) were exposed to all three Conditions, after which their permeable voids were measured following
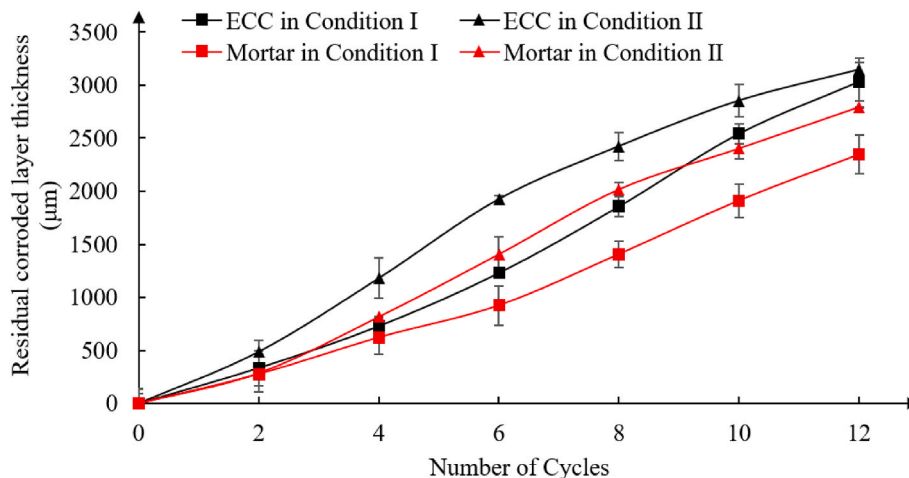

Fig. 8. Residual corroded layer thickness of the specimens increases with corrosion cycles, specimens under Condition III were not included in this plot because there was no corrosion layer.
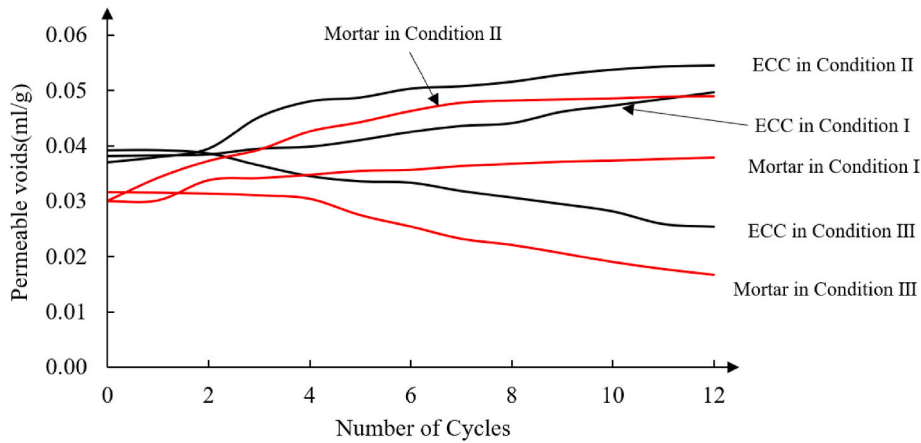
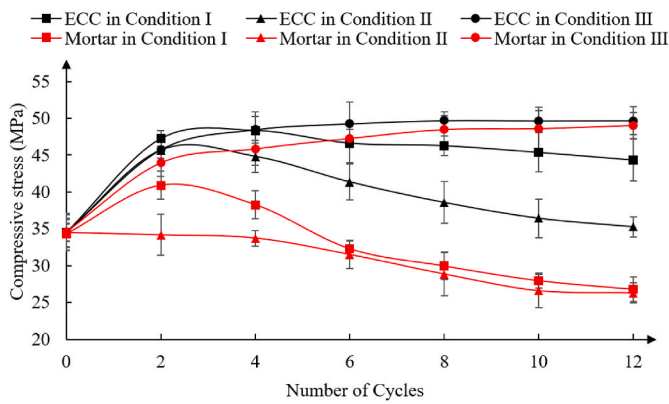Fig. 9. Permeable voids of specimens in response to exposure cycles.

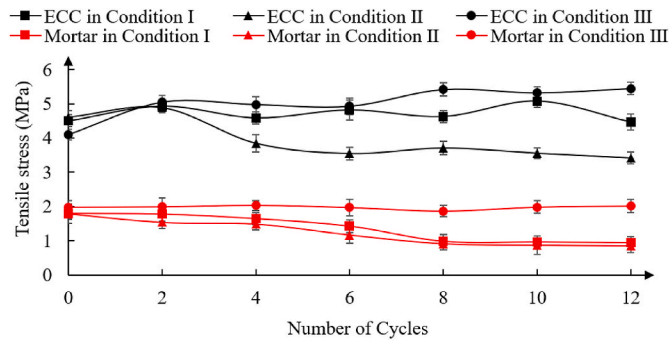Fig. 10. Compressive strength evolution with exposure cycles.

Fig. 11. Ultimate tensile strength evolution with exposure cycles.
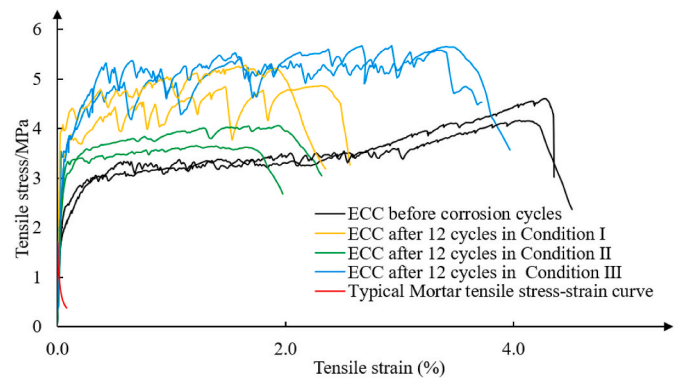

Fig. 12. Tensile stress-strain curve of ECC specimens without exposure and after 12 corrosive cycles of exposures. A typical tensile stress-strain curve of mortar specimens exposed to all conditions serve as a reference.

Table 5
Tensile properties of ECC specimens.

Exposure	First crack strength (MPa)	Tensile strength (MPa)	Tensile strain capacity (%)
Before cycles	3.05 ± 0.02	4.1 ± 0.2	4.20 ± 0.09
12 cycles in Condition I	3.83 ± 0.2	5.04 ± 0.18	2.18 ± 0.19
12 cycles in Condition II	3.57 ± 0.13	3.78 ± 0.22	1.94 ± 0.11
12 cycles in Condition III	4.70 ± 0.09	5.66 ± 0.13	3.49 ± 0.08

ASTM C642. Fig. 9 presents the measured permeable voids as a function of exposure cycles.

The ECC specimens revealed larger initial (Cycle 0) permeable voids because of fiber incorporation [61]. A reduction of permeable voids was observed under Condition III, presumably resulting from the continued cement hydration under tap water [40]. Under corrosive cycles, however, the ECC specimens had a big increase in permeable voids (30.5% in Condition I, and 47.6% in Condition II after 12 cycles). The corroded layers with high permeable voids under Condition I were thinner compared to the specimens exposed to Condition II which led to lower permeable void under Condition I [62].

The permeable voids of mortar specimens increased by 26.5% and 63.3% after 12 cycles in Condition I and II, respectively.

The difference in permeable voids of ECC specimens between Condition I and II was smaller than that of the mortar specimens suggesting that ECC specimens were less affected by the simulated corrosive-erosive sewage environment near the waterline.

3.3. Compressive strength

Fig. 10 shows the evolution of the compressive strength of cube specimens under the three exposure conditions. Except for mortar in Condition II, a rapid increase in the first two cycles was observed in corrosive environments and tap water. The initial increase of the compressive strength suggested that cement hydration played a dominant role under the corrosive environments in this period. After that, the strength grew slowly in tap water while strength loss became apparent under corrosive conditions. Moreover, no obvious compressive strength increase of the mortar specimens under Condition II was observed during the twelve cycles. Compressive strength loss occurs when the
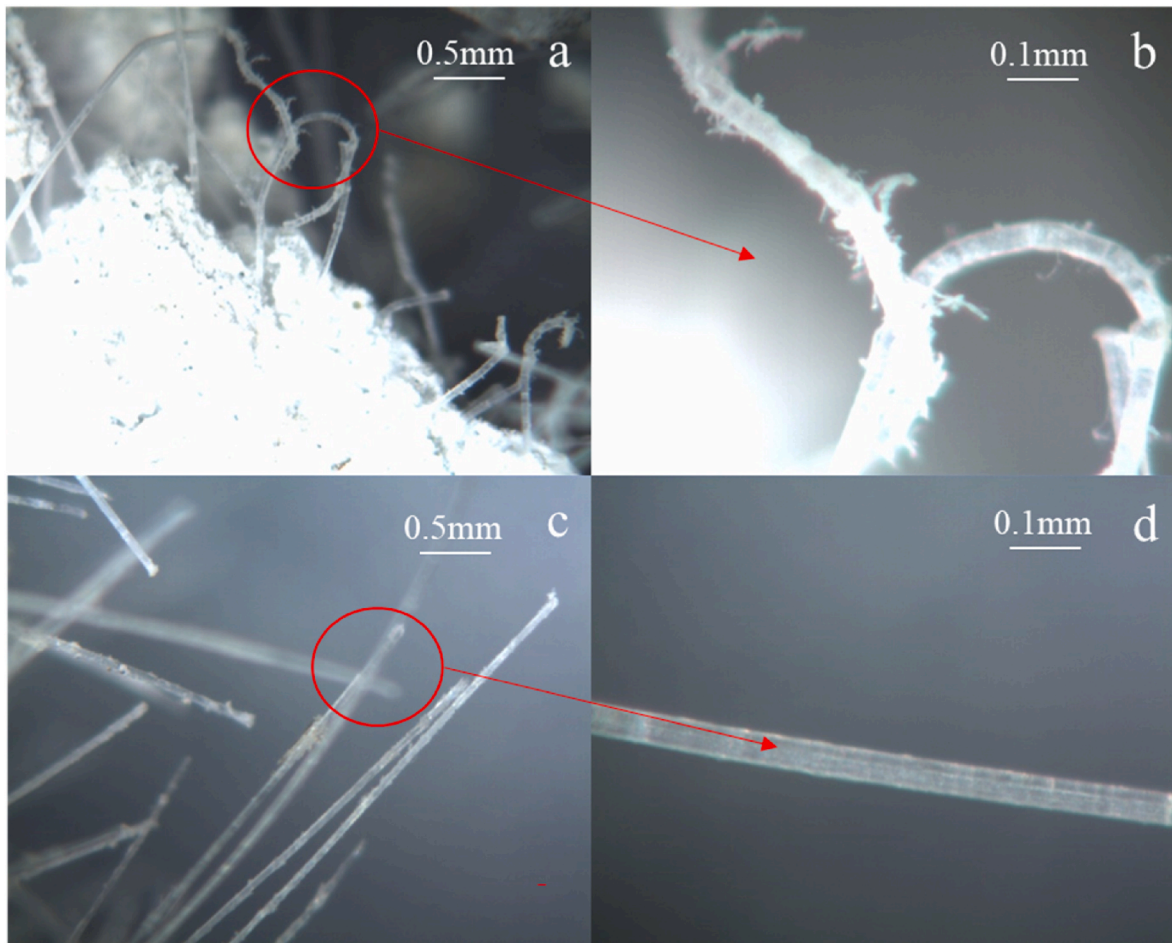
Fig. 13. Images taken by Infinity X–C21 electron microscope showing (a, b) curly PVA fibers after 12 cycles under Conditions I and II, and (c, d) straight PVA fibers after 12 cycles under Condition III.
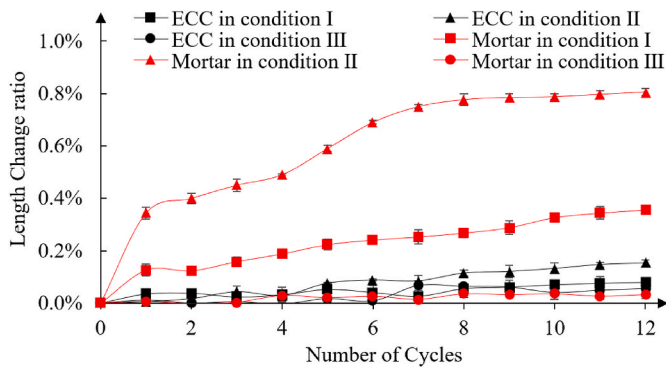

Fig. 14. ECC group demonstrates enhanced dimensional stability under all exposure conditions.

dissolution of the hydration products and the micro-cracking caused by the expansive corrosion product (gypsum) dominate over the effect of continued hydration [63].

More specifically, the compressive strengths of ECC and mortar specimens increased by 44.13%% and 41.76% after 12 cycles of Condition III exposure. After 2 cycles under Condition II, ECC specimens' compressive strength increased by 32.49% and then gradually decreased by 22.82% till the 12th cycle. Under Condition I, ECC's compressive strength increased by 37.02% in the first 2 cycles and then slightly decreased by 6.16% after 12 cycles. For ECC specimens, an initial rise in the second or third cycles is followed by a gradual loss of strength but retained a compressive strength increase of 28.58% and 2.26% above the initial level, under Conditions I and II, respectively. For mortar specimens, the compressive strength was reduced by 21.93% and 23.77% under 12 cycles of Conditions I and II exposures, respectively. The compressive strength of the ECC group was 65.4% and 34.2% higher than that of the mortar group under the same conditions. This indicated that the compressive strength of ECC specimens was better protected under simulated corrosive sewage environments compared to the mortar specimens. It also revealed that ECC's resistance to the simulated sewage environments was significantly higher than that of normal mortar/concrete with the same matrix [64].

3.4. Uniaxial tensile behavior

Uniaxial tension test was conducted on dogbone specimens after all three exposure conditions. The initial tensile strength of ECC was 107.1%–157.5% higher than that of the mortar specimens (Fig. 11). The tensile strength of mortar specimens decreased by 47.2% and 52.5% after 12 cycles under Conditions I and II and remained almost constant under Condition III. As for ECC specimens, the tensile strength decreased by 25.8% under Condition II and only 0.7% under Condition I. After 12 cycles, the tensile strength of ECC specimens was 370.53%, 302.35% and 171.14% higher than the mortar specimens under Condition I, II and III, respectively. ECC showed much higher tensile strength before and after corrosion cycles than mortar specimens which was an obvious advantage of ECC over the control mortar material.

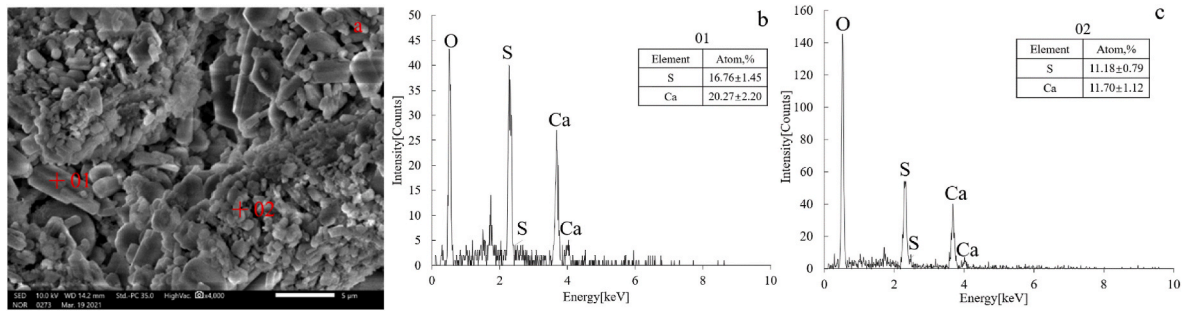The tensile stress-strain curve provides another important indicator

Fig. 15. (a) SEM images and (b and c) EDS results indicate the presence of gypsum crystals (Atom, %, Ca:S was similar to 1:1) in the corroded ECC and mortar specimens at two positions (marked in (a)).
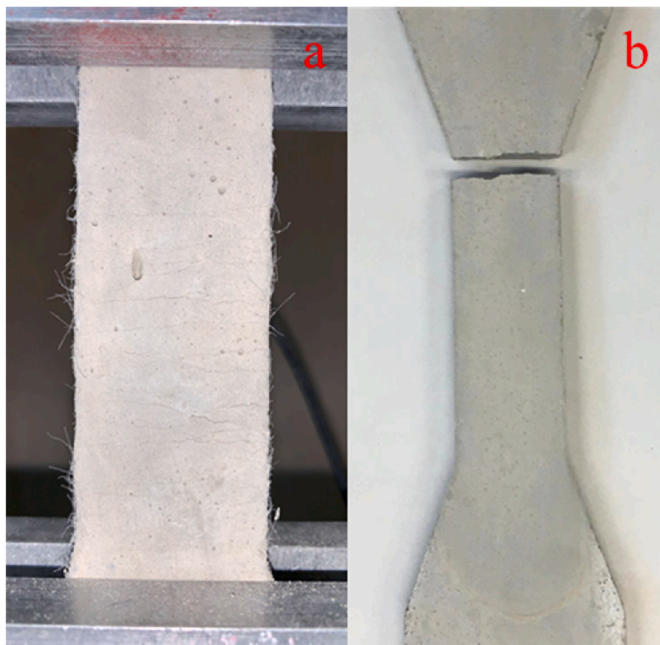

Fig. 16. a) ductile ECC specimens had multiple microcracks and continues to carry tensile load even at strain of 1% or more, b) brittle mortar specimens lost the tensile stress capacity and failed at the strain level less than 0.02%, accompanied by a single crack with indefinite width.

Table 6
RF recovery ratio of ECC dogbone specimens before exposure and after 2 exposure cycles.

Conditions	$RF_{control}$ (Hz)	Before exposure		After exposure	
		$RF_{cracked}$ (Hz)	$RF_{cracked}/$ $RF_{control}$	$RF_{cracked}$ (Hz)	$RF_{cracked}/$ $RF_{control}$
I	2199	1696	77.13%	2173	98.82%
II	2094	1590	75.93%	2067	98.71%
III	2226	1696	76.19%	2014	90.48%

$RF_{control}$: Initial RF value of control specimens (with no preloading).
$RF_{cracked}$: Initial RF value of cracked specimens.

to evaluate the properties of ECC materials [65] that may be affected by the corrosive environment. Fig. 12 shows the tensile stress-strain curve of ECC specimens after 12 cycles in corrosive conditions, which confirms the retaining of the unique high tensile ductility and strain-hardening performance of ECC [66] even after exposure to the harsh corrosive conditions. The tensile strain-hardening was accompanied by multiple cracking reflecting the multiple load-drops in the stress-strain curves for the ECC specimens. Despite a reduction in strain capacity caused by

exposure to the corrosion cycles, the ECC specimens remarkably retained about 50% of the tensile strain capacity, at about 2%. In contrast, the mortar specimens exposed to all conditions experienced an abrupt load drop after a minimal strain (less than 0.02%) (Fig. 12), reflecting its well known brittle failure mode even without exposure to the corrosive environments.

The tensile properties of ECC specimens are summarized in Table 5. The first crack strength increased by 54.1% and 25.6% after 12 cycles under Conditions III and I, respectively, while the tensile strain decreased by 16.9% in Condition III and 43.3% in Condition I. Under Condition II, the first crack strength increased by 17.0%, while the tensile strain decreased by 53.8%.

Fig. 13 shows the microscopic images of PVA fibers on the tensile fracture surface of the dogbone-shaped specimens. The pulled-out fibers under Conditions I and II were curly with notable abrasion and peeled-off fibrils on the surface (Fig. 13 a,b). In contrast, the protruded fibers in specimens under Condition III appear to be straight and smooth with nearly no damage on the fiber surface (Fig. 13 c, d). In addition to the dissolution of cement hydration products, the observed damage of the PVA fibers caused by acid exposure was also responsible for the observed loss of tensile strain capacity under Conditions I and II [41,67].

3.5. Length change

Over the 12 cycles, the length of mortar prism specimens (25 × 25 × 300 mm) under Condition I and II increased by 0.36% and 0.81%, while the expansion of ECC specimens was limited to below 0.08% and 0.15% under the same Conditions (Fig. 14).

Gypsum crystals were found in both corroded ECC and mortar specimens as revealed under SEM and confirmed by EDS elemental analysis (Fig. 15). The pressure created by gypsum crystal growth led to tensile stress and microcracks at the micro-scale [68,69] and resulted in the material expansion at the macro-scale. However, the expansion of ECC was only 22.22% and 18.52% of the mortars under Conditions I and II, suggesting that fiber bridging in ECC was able to mitigate the material expansion and micro-cracking. This is consistent with the compression test results (Section 3.3). Hence, ECC has better dimensional stability than mortar under corrosive environments.

3.6. Self-healing performance

Fig. 16a showed the ductility and multiple cracks on ECC specimens at the strain level of 1% while preloading. The mortar specimens fractured into two parts at about 0.02% strain (Fig. 16b). The crack width in mortar specimens increased indefinitely [65] showing negligible self-healing capacity [70]. In contrast, self-healing of microcracks was observed for ECC specimens under all conditions. Therefore, only ECC dogbone specimens preloaded in tension were examined using RF testing and optical microscopy examination. After dropping to 75.93%–77.13% (of the non-cracked specimen) on preloading to a tensile strain of 1%, the RF values of ECC samples recovered to 98.82%, 98.71% and
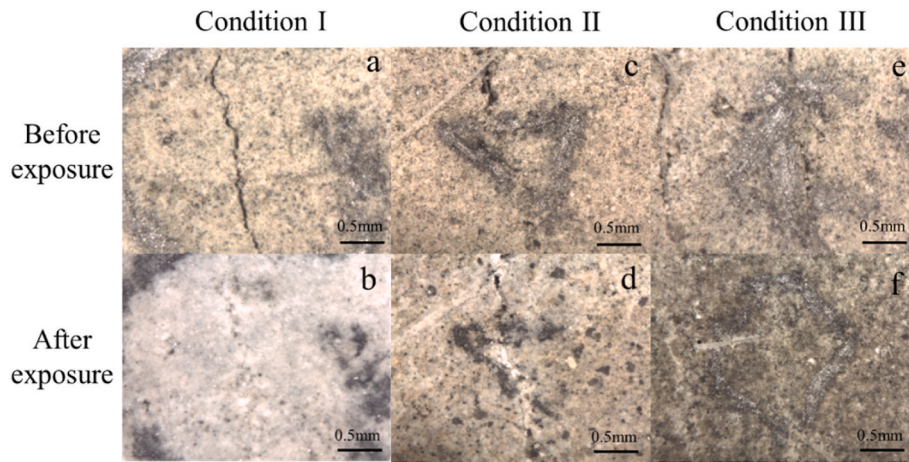
Fig. 17. Optical microscopy of crack sealing under all curing conditions. (a, c, e) Before exposure to Conditions I, II and III, and (b, d, f) after exposure to Conditions I and II and III.
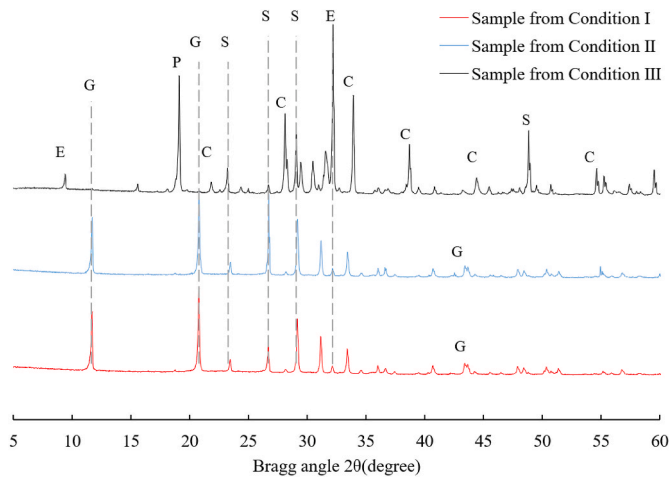

Fig. 18. XRD results of self-healing product (E: ettringite, G: gypsum, P: Ca(OH)$_2$, S: quartz, C: CaCO$_3$) from ECC samples after each of the three exposure conditions.

Fig. 20. Tensile stress-strain curve of pre-cracked (to 1% strain) ECC dogbone specimens after self-healing recovery from corrosive environments. The reference curve (labelled "Before cycles" is for a ECC specimen without preloading or exposure to cycles.
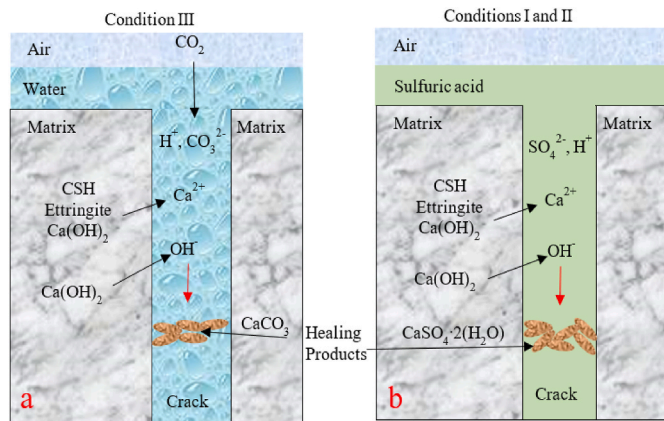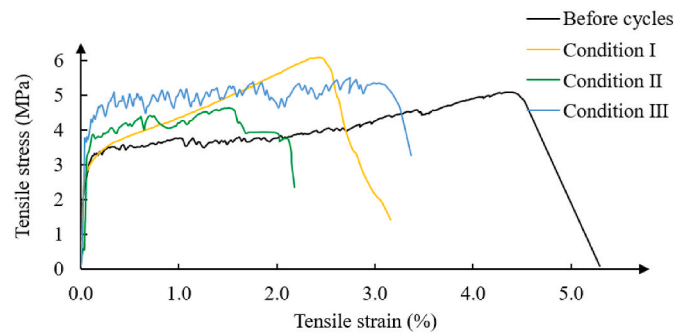

Fig. 19. Schematics of crack self-healing process under different exposure conditions, showing formation of a) CaCO$_3$ under Condition III and b) CaSO$_4$·2(H$_2$O) under Condition I/II.

90.48% of the non-cracked references after two cycles of exposure under Conditions I, II and III, respectively (Table 6). The recovery of RF value under the coupled influence of deterioration and crack sealing in ECC specimens suggests the ability of ECC to retain integrity [71] even in simulated aggressive sewage environments, and even when it was micro-cracked.

Fig. 17 shows the microcrack images of ECC specimens before exposure and after the three different exposure conditions. The sealing of microcracks is evident. This phenomenon has been verified to be beneficial to durability of concrete infrastructure [65]. The self-healing products and the surrounding uncracked materials were sampled for XRD. Fig. 18 shows the XRD patterns of samples from Conditions I, II and III. Under Condition III, calcite (CaCO$_3$, at Bragg angles 21.9, 28.1, 33.9, 38.7, 44.4, 54.5) was identified as the main self-healing products [40, 72]. Ca(OH)$_2$ (19.1) and ettringite (9.3 and 32.2) were also found in the samples from Condition III. For Condition I and II, the absence of peaks at 9.4, 19.1, 21.9, 28.1, 32.2, 33.9, 38.7, 44.4 and 54.5 suggests the dissolutions of ettringite, Ca(OH)$_2$ and CaCO$_3$ by the acid condition (Fig. 18). Peaks showed up at 11.7, 20.7 and 43.3 indicating that the corrosion product (gypsum) was the main self-healing product under Condition I and II. The growing crystals of CaCO$_3$ under Condition III and the gypsum formation under Condition I and II are responsible for sealing the cracks (Fig. 17) and the recovery of RF (Table 6).

The self-healing process is schematically illustrated in Fig. 19, based on the XRD and RF results. Under Condition III, the dissolved CO$_2$ from air generated CO$_3^{2-}$ and tiny amounts of H$^+$ in the water inside the cracks, while the CSH, ettringite, Ca(OH)$_2$ and CaCO$_3$ in the matrix

released Ca^{2+} to the water in the crack [72]. Eventually, the $CaCO_3$ filled in the cracks and contributed to the RF recovery under Condition III. Under Condition I and II, however, the healing mechanism was different. The acid solution under Condition I and II made it difficult for the CO_2 to enter the crack solution. The sulfuric acid provided a large amount of H^+ and SO_4^{2-} to the crack solution, which led to the formation of the $CaSO_4 \bullet 2(H_2O)$ together with the Ca^{2+} and OH^- from the matrix. Moreover, the higher concentration of H^+ under Condition I and II released more Ca^{2+} from the matrix. Hence, the recovered RF value was higher under Condition I and II compared to Condition III. The self-healing products filled or even sealed the cracks and contributed to the mechanical performance recovery of ECC under corrosive environments [41].

After self-healing and upon reloading in direct tension, the pre-cracked ECC specimens retained tensile strain-hardening behavior with strain capacities of 2.5%, 1.6% and 3.1% after exposure to environments under Conditions I, II and III, respectively (Fig. 20).

Based on the results of RF studies, optical microscopy observations, XRD analyses, and direct tension testing as documented in this Section, the self-healing phenomenon of pre-cracked ECC exposed to corrosive environments is confirmed.

4. Conclusions

The durability of ECC and fiber-free mortar was studied under simulated sewer environments considering the combined effects of sulfuric acid, $Na_2SO_4/Na_2S_2O_3$ solution, wet-dry cycles, and surface erosion. ECC demonstrated enhanced mechanical integrity and surface appearances compared to mortar due to its tensile strain-hardening capability. The difference of the final measured corroded layer thickness between Condition I (combined acid corrosion and erosion at the sewage waterline region) and Condition II (only acid corrosion at the crown region) is 72.7% less in the ECC group compared to that in the mortar control group. This reflects the superior ability of ECC over normal mortar/concrete in resisting spall damage under the most severe corrosive environment in sewage pipelines. The length expansion of the ECC specimens under the same exposure conditions was below 25% that of the mortar control group.

The technical properties of ECC were better retained compared to the reference mortar after the simulated sewage environmental exposures. The compressive strength and tensile strength of ECC were 30–65% and 300% higher, respectively, than the reference mortar after exposure. ECC retained good tensile ductility of over 2% (200 times that of traditional concrete) while maintaining self-healing ability.

In all, ductile ECC shows better physical and mechanical properties, reduced erosion tendency, and improved dimensional stability under simulated corrosive sewer environments when compared with mortar materials. It is concluded that ECC can contribute to a longer service life under simulated sewer pipe environments.

The research findings reported here warrants additional investigations into the tailoring of matrix composition for ECC for optimal resistance to corrosive environments in sewage pipes. A biogenic acid test that better emulates sewer line in-situ conditions and field tests of ECC sewer lines is needed.

Declaration of competing interest

The authors declare that they have no known competing financial interests or personal relationships that could have appeared to influence the work reported in this paper.

Acknowledgement

References

[1] C.D. Parker, Mechanics of corrosion of concrete sewers by hydrogen sulfide, Sewage Ind. Wastes (1951) 1477–1485.

[2] C. Grengg, F. Mittermayr, A. Baldermann, M.E. Böttcher, A. Leis, G. Koraimann, P. Grunert, M. Dietzel, Microbiologically induced concrete corrosion: a case study from a combined sewer network, Cement Concr. Res. 77 (2015) 16–25.

[3] V. Kaushal, M. Najafi, J. Love, Qualitative investigation of microbially induced corrosion of concrete in sanitary sewer pipe and manholes, Proc. ASCE Pipelines (2018) 768–775.

[4] A. Grandclerc, P. Dangla, M. Gueguen-Minerbe, T. Chaussadent, Modelling of the sulfuric acid attack on different types of cementitious materials, Cement Concr. Res. 105 (2018) 126–133.

[5] R. Singleton, The sulfate-reducing bacteria: an overview, in: The Sulfate-Reducing Bacteria: Contemporary Perspectives, Springer, New York, NY, 1993, pp. 1–20.

[6] US EPA, Hydrogen Sulfide Corrosion in Wastewater Collection and Treatment System, 1991.

[7] D.J. Roberts, D. Nica, G. Zuo, J.L. Davis, Quantifying microbially induced deterioration of concrete: initial studies, Int. Biodeterior. Biodegrad. 49 (4) (2002) 227–234.

[8] W. Sand, E. Bock, Concrete corrosion in the Hamburg sewer system, Environ. Technol. 5 (12) (1984) 517–528.

[9] H. Yuan, P. Dangla, P. Chatellier, T. Chaussadent, Degradation modeling of concrete submitted to biogenic acid attack, Cement Concr. Res. 70 (2015) 29–38.

[10] M.W. House, Using Biological and Physico-Chemical Test Methods to Assess the Role of Concrete Mixture Design in Resistance to Microbially Induced Corrosion, Purdue University, 2013.

[11] X. Sun, Improving the Understanding of Concrete Sewer Corrosion through Investigations of the Gaseous Hydrogen Sulfide Uptake and Transformation Processes in the Corrosion Layer, 2015.

[12] G.W. Scherer, Stress from crystallization of salt, Cement Concr. Res. 34 (9) (2004) 1613–1624.

[13] B. Huber, H. Hilbig, J.E. Drewes, E. Müller, Evaluation of concrete corrosion after short-and long-term exposure to chemically and microbially generated sulfuric acid, Cement Concr. Res. 94 (2017) 36–48.

[14] J. Monteny, E. Vincke, A. Beeldens, N. De Belie, L. Taerwe, D. Van Gemert, W. Verstraete, Chemical, microbiological, and in situ test methods for biogenic sulfuric acid corrosion of concrete, Cement Concr. Res. 30 (4) (2000) 623–634.

[15] W. Sand, Importance of hydrogen sulfide, thiosulfate, and methylmercaptan for growth of thiobacilli during simulation of concrete corrosion, Appl. Environ. Microbiol. 53 (7) (1987) 1645–1648.

[16] T. Wang, K. Wu, L. Kan, M. Wu, Current understanding on microbiologically induced corrosion of concrete in sewer structures: a review of the evaluation methods and mitigation measures, Construct. Build. Mater. 247 (2020) 118539.

[17] M. Wu, T. Wang, K. Wu, L. Kan, Microbiologically induced corrosion of concrete in sewer structures: a review of the mechanisms and phenomena, Construct. Build. Mater. 239 (2020) 117813.

[18] M.P. Lavigne, A. Bertron, L. Auer, G. Hernandez-Raquet, J.N. Foussard, G. Escadeillas, A. Cockx, E. Paul, An innovative approach to reproduce the biodeterioration of industrial cementitious products in a sewer environment. Part I: test design, Cement Concr. Res. 73 (2015) 246–256.

[19] R.D. Pomeroy, Process Design Manual for Sulfide Control in Sanitary Sewerage Systems, US Environmental Protection Agency, Technology Transfer, 1974.

[20] W.E. Shook, L.W. Bell, Corrosion Control in Concrete Pipe and Manholes, Technical Presentation, Water Environmental Federation, Florida, 1998.

[21] T. Mori, T. Nonaka, K. Tazaki, M. Koga, Y. Hikosaka, S. Noda, Interactions of nutrients, moisture and pH on microbial corrosion of concrete sewer pipes, Water Res. 26 (1) (1992) 29–37.

[22] M. O'Connell, C. McNally, M.G. Richardson, Biochemical attack on concrete in wastewater applications: a state of the art review, Cement Concr. Compos. 32 (7) (2010) 479–485.

[23] M. House, W.J. Weiss, Review of Microbially Induced Corrosion and Comments on Needs Related to Testing Procedures, 2014.

[24] J. Monteny, N. De Belie, E. Vincke, W. Verstraete, L. Taerwe, Chemical and microbiological tests to simulate sulfuric acid corrosion of polymer-modified concrete, Cement Concr. Res. 31 (9) (2001) 1359–1365.

[25] M. House, L. Cheng, K. Banks, J. Weiss, Concrete resistance to sulfuric acid immersion: the influence of testing details and mixture design on performance as it relates to microbially induced corrosion, Adv. Civ. Eng. Mater. 8 (1) (2019) 544–557.

[26] B. Li, F. Wang, H. Fang, K. Yang, X. Zhang, Y. Ji, Experimental and Numerical Study on Polymer Grouting Pretreatment Technology in Void and Corroded Concrete Pipes, Tunnelling and Underground Space Technology, 2021, p. 103842.

[27] T. Wang, L. Tan, S. Xie, B. Ma, Development and applications of common utility tunnels in China, Tunn. Undergr. Space Technol. 76 (2018) 92–106.

[28] F. Saucier, J. Herisson, Use of Calcium Aluminate Cement in H_2S Biogenic Environment, Institute of Concrete Technology, Yearbook, 2015, pp. 67–80, 2015–2016.

[29] T. Noeiaghaei, A. Mukherjee, N. Dhami, S.R. Chae, Biogenic deterioration of concrete and its mitigation technologies, Construct. Build. Mater. 149 (2017) 575–586.

[30] M.L. Berndt, Evaluation of coatings, mortars and mix design for protection of concrete against sulphur oxidising bacteria, Construct. Build. Mater. 25 (10) (2011) 3893–3902.

[31] S.Y. Alam, R. Zhu, A. Loukili, A new way to analyse the size effect in quasi-brittle materials by scaling the heterogeneity size, Eng. Fract. Mech. 225 (2020) 106864.

[32] P.K. Mehta, P.J. Monteiro, Concrete Microstructure, Properties and Materials, 2017.

[33] D. Shen, C. Liu, C. Li, X. Zhao, G. Jiang, Influence of Barchip fiber length on early-age behavior and cracking resistance of concrete internally cured with super absorbent polymers, Construct. Build. Mater. 214 (2019) 219–231.

[34] V.C. Li, Performance Driven Design of Fiber Reinforced Cementitious Composites, 1992.

[35] M.D. Lepech, V.C. Li, Water permeability of engineered cementitious composites, Cement Concr. Compos. 31 (10) (2009) 744–753.

[36] H. Liu, Q. Zhang, C. Gu, H. Su, V.C. Li, Influence of micro-cracking on the permeability of engineered cementitious composites, Cement Concr. Compos. 72 (2016) 104–113.

[37] G.P. van Zijl, F.H. Wittmann, B.H. Oh, P. Kabele, R.D. Toledo Filho, E.M. Fairbairn, V. Slowik, A. Ogawa, H. Hoshiro, V. Mechtcherine, F. Altmann, M.D. Lepech, Durability of strain-hardening cement-based composites (SHCC), Mater. Struct. 45 (10) (2012) 1447–1463.

[38] M. Şahmaran, V.C. Li, Durability properties of micro-cracked ECC containing high volumes fly ash, Cement Concr. Res. 39 (11) (2009) 1033–1043.

[39] H. Liu, Q. Zhang, V. Li, H. Su, C. Gu, Durability study on engineered cementitious composites (ECC) under sulfate and chloride environment, Construct. Build. Mater. 133 (2017) 171–181.

[40] H.L. Wu, D. Zhang, Y.J. Du, V.C. Li, Durability of engineered cementitious composite exposed to acid mine drainage, Cement Concr. Compos. 108 (2020) 103550.

[41] M. Ohno, V.C. Li, Sulfuric acid resistance of strain hardening fiber reinforced geopolymer composite, Indian Concr. J. 12 (2019) 47–53.

[42] H. Liu, Q. Zhang, C. Gu, H. Su, V. Li, Self-healing of microcracks in Engineered Cementitious Composites under sulfate and chloride environment, Construct. Build. Mater. 153 (2017) 948–956.

[43] E.K. Attiogbe, S.H. Rizkalla, Response of concrete to sulfuric acid attack, ACI Mater. J. 85 (6) (1988) 481–488.

[44] V. Pavlík, Corrosion of hardened cement paste by acetic and nitric acids part II: formation and chemical composition of the corrosion products layer, Cement Concr. Res. 24 (8) (1994) 1495–1508.

[45] People's Republic of China Building Materials Industry Standard. Concrete and Reinforced Concrete Pipes (GB/11836-2009) [S],China National Standardization Management Committee.

[46] ASTM, ASTM C150: Standard Specification for Portland Cement, ASTM, Philadelphia˙ ePA PA, 2001.

[47] ASTM Standard C618-08a, Standard Specification for Coal Fly Ash and Raw or Calcined Natural Pozzolan for Use in Concrete, Annual Book of ASTM Standards, ASTM International, West Conshohocken, PA, 2008.

[48] ASTM C490/C490M-17, Standard Practice for Use of Apparatus for the Determination of Length Change of Hardened Cement Paste, Mortar, and Concrete, ASTM International, *West Conshohocken*, PA, 2017.

[49] A. Attal, M. Brigodiot, P. Camacho, J. Manem, Biological mechanisms of H_2S formation in sewer pipes, Water Sci. Technol. 26 (3–4) (1992) 907–914.

[50] T.A. Durning, M.C. Hicks, Using microsilica to increase concrete's resistance to aggressive chemicals, Concr. Int. 13 (3) (1991) 42–48.

[51] T. Wells, R.E. Melchers, P. Bond, Factors Involved in the Long Term Corrosion of Concrete Sewers, Australasian corrosion association proceedings of corrosion and prevention, Coffs Harbour, Australia, 2009, p. 11.

[52] ASTM C642-13, Standard Test Method for Density, Absorption, and Voids in Hardened Concrete, ASTM International, West Conshohocken, PA, 2013.

[53] ASTM C109/C109M, Standard Test Method for Compressive Strength of Hydraulic Cement Mortars, 2013.

[54] Rokugo K. Chair, JSCE, in: Recommendations for Design and Construction of High Performance Fiber Reinforced Cement Composites with Multiple Fine Cracks (HPFRCC). Concrete Committee, Japan Society of Civil Engineers, March, 2008, p. 212.

[55] Y. Yang, E.H. Yang, V.C. Li, Autogenous healing of engineered cementitious composites at early age, Cement Concr. Res. 41 (2) (2011) 176–183.

[56] ASTM C215/C215M, Standard Test Method for Fundamental Transverse, Longitudinal, and Torsional Resonant Frequencies of Concrete Specimens, 2014.

[57] D. Zhang, B. Jaworska, H. Zhu, K. Dahlquist, V.C. Li, Engineered Cementitious Composites (ECC) with limestone calcined clay cement (LC3), Cement Concr. Compos. 114 (2020) 103766.

[58] N. Roghanian, N. Banthia, Development of a sustainable coating and repair material to prevent bio-corrosion in concrete sewer and waste-water pipes, Cement Concr. Compos. 100 (2019) 99–107.

[59] Y. Xie, X. Lin, T. Ji, Y. Liang, W. Pan, Comparison of corrosion resistance mechanism between ordinary Portland concrete and alkali-activated concrete subjected to biogenic sulfuric acid attack, Construct. Build. Mater. 228 (2019) 117071.

[60] V. Pavlík, Corrosion of hardened cement paste by acetic and nitric acids part II: formation and chemical composition of the corrosion products layer, Cement Concr. Res. 24 (8) (1994) 1495–1508.

[61] C.C. Thong, D.C.L. Teo, C.K. Ng, Application of polyvinyl alcohol (PVA) in cement-based composite materials: a review of its engineering properties and microstructure behavior, Construct. Build. Mater. 107 (2016) 172–180.

[62] L.W. Bell, W.E. Shook, T. Norris, Mitigating the corrosion of concrete pipe and manholes, in: Concrete Pipe for the New Millennium, ASTM International, 2000.

[63] W. Müllauer, R.E. Beddoe, D. Heinz, Sulfate attack expansion mechanisms, Cement Concr. Res. 52 (2013) 208–215.

[64] M. Hlobil, V. Šmilauer, G. Chanvillard, Micromechanical multiscale fracture model for compressive strength of blended cement pastes, Cement Concr. Res. 83 (2016) 188–202.

[65] V.C. Li, Engineered Cementitious Composites (ECC): Bendable Concrete for Sustainable and Resilient Infrastructure, Springer, 2019.

[66] V.C. Li, F.P. Bos, K. Yu, W. McGee, T.Y. Ng, S.C. Figueiredo, P.J. Kruger, On the emergence of 3D printable engineered, strain hardening cementitious composites (ECC/SHCC), Cement Concr. Res. 132 (2020) 106038.

[67] I. Curosu, M. Liebscher, G. Alsous, E. Muja, H. Li, A. Drechsler, V. Mechtcherine, Tailoring the crack-bridging behavior of strain-hardening cement-based composites (SHCC) by chemical surface modification of poly (vinyl alcohol) (PVA) fibers, Cement Concr. Compos. 114 (2020) 103722.

[68] D. Zhang, B. Jaworska, Effect of carbonation curing on Portland cement $MgSO_4$ attack: laboratory characterization at 900 days, J. Mater. Civ. Eng. 33 (4) (2021), 04021032.

[69] D. Zhang, V.C. Li, B.R. Ellis, Ettringite-related dimensional stability of CO2-cured Portland cement mortars, ACS Sustain. Chem. Eng. 7 (19) (2019) 16310–16319.

[70] Gürkan Yıldırım, , Özlem Kasap Keskin, Süleyman Bahadır Keskin, Mustafa Şahmaran, Mohamed Lachemi, A review of intrinsic self-healing capability of engineered cementitious composites: recovery of transport and mechanical properties, Construct. Build. Mater. 101 (2015) 10–21.

[71] Y. Yang, M.D. Lepech, E.H. Yang, V.C. Li, Autogenous healing of engineered cementitious composites under wet–dry cycles - sciencedirect, Cement Concr. Res. 39 (5) (2009) 382–390.

[72] D. Zhang, Z. Ghouleh, Y. Shao, Review on carbonation curing of cement-based materials, J. CO2 Util. 21 (2017) 119–131.